Monthly Notices
of the
ROYAL ASTRONOMICAL SOCIETY

MNRAS **480,** 1547–1562 (2018) doi:10.1093/mnras/sty1925

# New full evolutionary sequences of H- and He-atmosphere massive white dwarf stars using MESA

G. R. Lauffer,★ A. D. Romero and S. O. Kepler

*Instituto de Física, Universidade Federal do Rio Grande do Sul, Av. Bento Goncalves 9500, Porto Alegre 91501-970, RS, Brazil*

Accepted 2018 July 12. Received 2018 July 12; in original form 2018 May 4

## ABSTRACT

We explore the evolution of hydrogen-rich and hydrogen-deficient white dwarf stars with masses between 1.012 and 1.307 $M_\odot$, and initial metallicity of $Z = 0.02$. These sequences are the result of main-sequence stars with masses between 8.8 and 11.8 $M_\odot$. The simulations were performed with MESA (Modules for Experiments in Stellar Astrophysics), starting at the zero-age main sequence, through thermally pulsing and mass-loss phases, ending at the white dwarf cooling sequence. We present reliable chemical profiles for the whole mass range considered, covering the different expected central compositions (i.e. C/O, O/Ne and Ne/O/Mg) and its dependence on the stellar mass. In addition, we present detailed chemical profiles of hybrid C/O–O/Ne core white dwarfs, found in the mass range between 1.024 and 1.15 $M_\odot$. We present the initial-to-final mass relation, the mass–radius relation and cooling times considering the effects of atmosphere and core composition.

**Key words:** methods: numerical – stars: evolution – stars: white dwarfs.

## 1 INTRODUCTION

White dwarf stars are the most common final stage of stellar evolution. They are the end product of main-sequence stars with masses up to 5–12 $M_\odot$ (García-Berro, Isern & Hernanz 1997a; Poelarends et al. 2008; Siess 2010; Langer 2012; Woosley & Heger 2015; Doherty et al. 2015), depending on metallicity, which correspond to 95–97 % of all stars in the Galaxy. White dwarf stars are excellent galactic chronometers as they are slowly cooling, releasing the heat stored in the core. The age of stellar populations can be obtained by comparisons of theoretical computations with their distribution in the colour–magnitude diagram (Hansen et al. 2007; Campos et al. 2016) or from the white dwarf luminosity function (Winget et al. 1987; Bedin et al. 2010; García-Berro et al. 2014). The connection between the properties of progenitor stars and white dwarfs is depicted in the initial-to-final mass relation (IFMR), which leads to constraints on the upper mass limit that separates white dwarf progenitors of Type II supernovae (Siess 2007; Catalán et al. 2008). Also, binary systems with white dwarfs are believed to produce Type Ia supernovae as a result of accretion that exceeds the upper mass limit (e.g. Wang, Podsiadlowski & Han 2017). Finally, a comparison between models and observations of white dwarfs can enhance the comprehension of the physical properties of high-density matter (e.g. Prada Moroni & Straniero 2002; Isern et al. 2010).

White dwarf stars can be divided into two main classes, DA and non-DA types, based on the main component of their atmosphere. The DA spectral class shows a hydrogen-rich atmosphere and represent $\simeq$ 84 % of all white dwarfs (e.g. Kepler et al. 2007) while non-DA types have hydrogen-deficient atmospheres. The non-DA white dwarfs can be classified by the dominant element in their spectra and effective temperature: a DO class with strong lines of He II and effective temperatures of $T_{\rm eff} \approx 45\,000$–$200\,000$ K; a DB class with strong He I lines and $T_{\rm eff} \approx 11\,000$–$30\,000$ K; and for effective temperatures below $T_{\rm eff} \approx 11\,000$ K, DC, DQ and DZ classes with traces of carbon and metals in their spectra. The helium-rich white dwarfs are believed to be progeny of PG 1159 stars (McGraw et al. 1979) formed by a born-again episode (Schoenberner 1979; Iben et al. 1983) in which a helium flash occurs during the cooling sequence (i.e. very late thermal pulse) forcing the star to evolve back to the asymptotic giant branch (AGB). As a result, this very late thermal pulse burns out all hydrogen left in the atmosphere of the star.

White dwarfs with masses in the range 0.4–1.05 $M_\odot$ are believed to harbour a carbon/oxygen (C/O) core, after central hydrogen- and helium-burning in earlier stages of evolution. However, the progenitors of white dwarfs with masses larger than $\approx$1.05 $M_\odot$ (García-Berro et al. 1997a; Siess 2007) should reach a temperature high enough to achieve stable carbon-burning, forming an oxygen/neon (O/Ne) or neon/oxygen/magnesium (Ne/O/Mg) core, depending on whether carbon-burning ignites off-centre or at the centre of the star. When carbon-burning starts off-centre, ignition is followed by an inward propagation of the burning front (hereafter the carbon flame). This carbon flame might or might not reach the centre. If the flame does not reach the centre, then a hybrid C/O+O/Ne white dwarf will form (Denissenkov et al. 2013; Farmer, Fields & Timmes

★ E-mail: gabriel.lauffer@ufrgs.br

© 2018 The Author(s)
Published by Oxford University Press on behalf of the Royal Astronomical Society

Downloaded from https://academic.oup.com/mnras/article-abstract/480/2/1547/5065044 by Universidade Federal do Rio Grande do Sul user on 16 January 2019

2015), whilst a flame that does reach the centre will form a Ne/O/Mg white dwarf. These results are dependent on the evolutionary code and input physics considered. Siess (2007) calculated sequences for several metallicities, with and without overshooting, and found that for $Z = 0.02$ the minimum core mass for O/Ne cores is 1.04 $M_\odot$. Based on sequences calculated until the thermally pulsing asymptotic giant branch (TP-AGB) phase, Doherty et al. (2015) found that for $Z = 0.02$ the minimum core mass for an O/Ne core white dwarf star is 1.154 $M_\odot$. The determination of the mass range for each type of core composition is fundamental to improve our understanding of the populations of massive white dwarf stars.

The number of spectroscopically confirmed white dwarf stars has increased to more than $\approx$ 30 000 with surveys such as the Sloan Digital Sky Survey (SDSS; Ahn et al. 2014). The mass distribution for DA white dwarf stars presented by Kleinman et al. (2013) is centred at 0.649 $M_\odot$ but it presents another peak at 0.811 $M_\odot$ (Kepler et al. 2015). In addition, an analysis of 112 isolated massive white dwarfs performed by Należyty & Madej (2004) showed that, for known white dwarfs with masses $\geq$0.8 $M_\odot$, the mass distribution has a primary peak at $\approx$0.8 $M_\odot$ and a secondary peak around 1.04 $M_\odot$. Around 20 % of all DA white dwarfs are more massive than 0.8 $M_\odot$ (Liebert, Bergeron & Holberg 2005; Kepler et al. 2007) and about 9 % have mass around 1.12 $M_\odot$ (Kepler et al. 2007). Recent works have presented a high-mass tail on the mass distribution with an excess for masses around $M_{\rm WD} \approx 1.0$ $M_\odot$ (Falcon et al. 2010; Tremblay et al. 2013; Rebassa-Mansergas et al. 2015; Kepler et al. 2016).

In the literature, there are several evolutionary models for low- and intermediate-mass white dwarf stars. For instance, Romero et al. (2012, 2013) and Althaus et al. (2009) have studied C/O core DA and non-DA white dwarfs, respectively, and Althaus, Miller Bertolami & Córsico (2013), Istrate et al. (2014, 2016), Istrate, Fontaine & Heuser (2017) and Sun & Arras (2017) have studied low-mass and extremely low-mass white dwarfs. However, there is a lack of full evolutionary models for massive white dwarfs. Recently, some authors have computed the evolution of super-AGB stars until the end of the thermally pulsing phase (Siess 2010; Gil-Pons et al. 2013; Jones et al. 2013; Doherty et al. 2015), but they have not computed the following post-AGB stage or the white dwarf evolution. Other authors computed white dwarf models by generating static/politropic models at the top of the cooling sequence and/or by rescaling the mass and/or by artificially inserting a previously calculated chemical profile with fixed O/Ne ratios and fixed hydrogen and helium layers on the atmosphere (Benvenuto & Althaus 1999; Salaris et al. 2000; Althaus et al. 2005b, 2007; Salaris, Althaus & García-Berro 2013).

In this present work, we intend to fill the gap resulting from the lack of full evolutionary sequences for massive white dwarfs, computed from the zero age main-sequence (ZAMS) through the red giant branch (RGB) and AGB to the white dwarf cooling sequence. To this end, we used the MESA evolutionary code (Modules for Experiments in Stellar Astrophysics; Paxton et al. 2011, 2013, 2015, 2018). We computed full evolutionary sequences with initial masses in the range of 8.8–11.8 $M_\odot$ resulting in white dwarf models with masses in the range of 1.01–1.31 $M_\odot$, adding both hydrogen- and helium-rich envelopes. This paper is organized as follows. In Section 2, we present the MESA evolutionary code and the input physics considered in our computations. The results from our full evolutionary computations are presented in Section 3. In Section 4, we discuss the mass–radius relation of our sequences. Finally, we present our final remarks in Section 5.

## 2 NUMERICAL SIMULATIONS

The numerical simulations were performed using the MESA code (Paxton et al. 2011, 2013, 2015, 2018), version r8845. We started the computations on the ZAMS, considering an initial metallicity $Z = 0.02$. We computed the hydrogen-burning and helium-burning stages, and the RGB and AGB mass-loss phases. The sequences ended as C/O or O/Ne/Mg white dwarfs cooled to log $L/L_\odot \sim -4$, which represents $T_{\rm eff} \approx$ 7 000–10 000 K depending on the final mass.

The MESA evolutionary code has been extensively used to perform calculations of extremely low-mass white dwarfs (Istrate et al. 2016, 2017; Sun & Arras 2017), hybrid C/O/Ne white dwarfs and Type Ia supernova progenitors (Denissenkov et al. 2013; Jones et al. 2013; Chen et al. 2014; Farmer et al. 2015; Brooks et al. 2017a), accreting white dwarf binaries with C/O cores (Brooks et al. 2016; Wang et al. 2017) and O/Ne cores (Brooks et al. 2017b; Schwab, Bildsten & Quataert 2017), white dwarf isochrones (Dotter 2016) and sets of sequences covering the white dwarf mass range (Choi et al. 2016; Pignatari et al. 2016; Ritter et al. 2018).

We detail the input physics considered prior and during white dwarf evolution in the following subsections.

### 2.1 Pre-white-dwarf evolution

For the evolutionary phases prior to the cooling sequence, we considered the nuclear network `co_burn_plus.net`, which has 16 elements from hydrogen to silicon: $^{1}$H, $^{3,4}$He, $^{12,13}$C, $^{13-15}$N, $^{16-18}$O, $^{19}$F, $^{20,22}$Ne, $^{24}$Mg and $^{28}$Si. This network has 67 nuclear reactions, including pp-chain, CNO cycle, triple-alpha and some auxiliary reactions. We used the Joint Institute for Nuclear Astrophysics (JINA) REACLIB database (Cyburt et al. 2010) with electron screening factors for thermonuclear reactions from Graboske et al. (1973) and DeWitt, Graboske & Cooper (1973) for weak and intermediate screening, and from Alastuey & Jancovici (1978) for the strong screening regime. Plasma parameters are those from Itoh et al. (1979). The energy-loss rates including the derivatives from thermal neutrinos are from Itoh et al. (1996). The equation of state (EOS) is based on the OPAL EOS tables (Rogers & Nayfonov 2002) including the Saumon–Chabrier–van Horn (SCvH) tables (Saumon, Chabrier & van Horn 1995) for lower temperatures and densities, and the HELM EOS (Timmes & Swesty 2000) and Potekhin–Chabrier (PC) EOS (Potekhin & Chabrier 2010) for higher temperatures and densities.

Convection was consider using the Ledoux criterion, which takes into account the composition gradient, along with the Cox implementation of mixing-length theory (MLT; Cox & Giuli 1968) with a mixing-length free parameter $\alpha_{\rm MLT} = 2$. The diffusion and gravitational settling in MESA are calculated by solving the equations from Burgers (1969) with coefficients of Thoul, Bahcall & Loeb (1994). In the overshoot region, MESA treats convective mixing as a time-dependent diffusion process, with a diffusion coefficient given by

$$D_{\rm OV} = D_{\rm conv,0} \exp -\frac{2z}{f\lambda_{\rm P,0}}, \quad (1)$$

where $D_{\rm conv,0}$ is the MLT-derived diffusion coefficient at the convective boundary, $z$ is the distance from the convective boundary, $\lambda_{\rm P,0}$ is the local pressure scale height and $f$ is the adjustable parameter (Herwig 2000), which can have different values at the upper and lower convective boundaries for H-burning, He-burning, metal-burning (i.e all burning regions that are not H- or



Downloaded from https://academic.oup.com/mnras/article-abstract/480/2/1547/5065044 by Universidade Federal do Rio Grande do Sul user on 16 January 2019

He-burning) and non-burning convection zones. Because of convergence issues, overshooting was only considered for the lower boundary of the metal-burning convective region with parameters set to `overshoot_f_below_burn_z_shell` = 0.1 and `overshoot_f0_below_burn_z_shell` = 0.01. The mixing in regions unstable to Schwarzschild criteria but stable to Ledoux criteria is treated by semiconvection (Langer, Fricke & Sugimoto 1983) using the dimensionless efficiency parameter $\alpha_{sc} = 0.01$. Thermohaline mixing (Ulrich 1972; Kippenhahn, Ruschenplatt & Thomas 1980) is also considered with the efficiency parameter set to $\alpha_{th} = 2$. For details of the implementation of semiconvection and thermohaline mixing, refer to Section 4 of Paxton et al. (2013).

Mass loss was considered during the giant phases (i.e. RGB and AGB phases). We used the mass-loss formula from Reimers (1975) with $\eta = 0.1$ during the RGB phase, followed by the Bloecker (1995) scheme with $\eta = 10$ in the AGB phase. The opacity tables are those from OPAL type 2 (Iglesias & Rogers 1996) for enhanced C/O variations in composition. We used a grey atmosphere for the entire evolution. Considering white dwarf stars have rotation periods of ∼1 d (Kepler & Romero 2017), in most cases, the effects of rotation are negligible. Even though there are a few known fast rotators, we do not consider rotation in our computations.

### 2.2 White dwarf evolution

Chemical diffusion and gravitational settling was modelled following the formulation from Burgers (1969). Sun & Arras (2017) suggested that the routine `diffusion_use_cgs_solver` is better suited for electron degeneracy, but they considered only very low-mass white dwarf models with stellar mass below $M_{WD} < 0.17\ M_\odot$. Employing this formulation for diffusion in massive models leads to numerical instabilities and to non-physical chemical profiles.

In our models, convection was shut down as a result of numerical instabilities during the cooling sequence. Computations with or without convection show no differences in the final ages of our cooling sequences. The same happens when the Sun & Arras (2017) formulation is considered. Thus, our treatment of diffusion and convection does not affect the cooling times in the mass range considered in this work.

The energy-loss rates from thermal neutrinos and its derivatives are from Itoh et al. (1996).

White dwarf stars are expected to undergo crystallization as a result of strong Coulomb interactions in their dense interiors (van Horn 1968). The transition occurs when the energy of the Coulomb interaction between neighbouring ions is much larger than their thermal energy. The ratio between these two contributions can be expressed as a coupling parameter $\Gamma = \bar{Z}^2 e^2 / a_i k_B T$, where $\bar{Z}$ is the average ion charge, $a_i$ is the mean ion spacing and the other symbols have their usual meaning. Crystallization for pure oxygen plasma begins when $\Gamma \approx 175$ (van Horn 1969). The onset of crystallization also depends on the adopted phase diagram. Near the crystallization limit ($\Gamma \sim 175$), MESA uses the PC EOS, which accounts for the thermodynamics of crystals. By default, MESA changes from the HELM EOS to the PC EOS when the Coulomb coupling parameter $\Gamma > 80$ and considers a mixture of solid and liquid for $\Gamma_i = 150$ and a full crystal when $\Gamma_{full} = 175$. These values were obtained by Potekhin & Chabrier (2010). Results from the asteroseismological analysis performed by Romero et al. (2013) indicate that the azeotropic type phase diagram from Horowitz, Schneider & Berry (2010) better represents the crystallization on white dwarfs cores (see also Schneider et al. 2012; Hughto et al. 2012). Hence, we modified the values for the coupling constant $\Gamma$ to $\Gamma_i = 215$ and $\Gamma_{full} = 220$ in our computations. Thus, the release of latent heat occurs for $\Gamma = 215-220$. This modification had to be done on the file `pc_eos.f` located inside MESA `eos` module. Until MESA version r8845, which is used in this work, there was no option to control those parameters.

The Debye cooling regime, which affects the cooling of white dwarfs at lower luminosities, was not considered in our simulations. However, this effect will not be important in our results, as it occurs for temperatures below ∼ 10 000 K and luminosities lower than $\log L/L_\odot < -4.06$ (Althaus et al. 2007) for the mass range considered in this work (see Section 3.6).

## 3 EVOLUTION FROM THE ZAMS TO THE COOLING CURVE

We calculated 16 full evolutionary sequences with initial metallicity $Z = 0.02$ and initial mass at the ZAMS between 8.80 and 11.80 $M_\odot$. As a result, we obtained white dwarf models with stellar masses ranging from 1.012 to 1.307 $M_\odot$. From our computations, we find that a sequence with an initial mass of 11.9 $M_\odot$ does not result in a white dwarf but possibly ends up as a neutron star. Thus, a white dwarf with the Chandrasekhar limiting mass should have a progenitor with an initial mass between 11.8 and 11.9 $M_\odot$. Further calculations are needed to determine the model that leads to the Chandrasekhar mass limit. Note that within this mass range there are two possible core compositions (i.e. C/O and O/Ne/Mg). At high stellar masses, our computations complement the works of Romero et al. (2012, 2013) who computed C/O core white dwarf sequences with masses below $M_{WD} = 1.050\ M_\odot$. Our H- and He-atmosphere sequences have evolved equally in the stages prior to the cooling sequence, so there is no distinction on the evolution previous to the white dwarf stage.

During the AGB phase, the computations present numerical difficulties related to the mass-loss episodes. At this stage, we use the mass-loss prescription of Bloecker (1995) with a factor $\eta = 10$, which leads to the complete removal of the hydrogen envelope, preventing the occurrence of thermal pulses, in all sequences. A less efficient mass-loss rate, achieved by decreasing the value of $\eta$, does not allow us to compute the stages following the AGB stage but it still leads to the complete removal of hydrogen. The same occurs for other MESA built-in mass-loss schemes. García-Berro et al. (1997a) discussed that a model with rapid radiative wind during the AGB phase is expected to lose all its hydrogen layer and most of its helium layer, leading to a PG 1159 star; however, real massive white dwarfs are known to have H and He envelopes. In order to produce hydrogen atmosphere white dwarf sequences, we artificially added hydrogen at the surface of the models. This procedure was performed at high effective temperatures, near the beginning of the cooling sequences, so the transitory effects caused by the artificial procedure are rapidly washed out. The amount of hydrogen added to each sequence was computed by a linear extrapolation to higher stellar mass of the results of Romero et al. (2012, 2013). The amount of hydrogen as a function of the white dwarf stellar mass is shown in Fig. 1. Circles correspond to the results from Romero et al. (2012, 2013), while the triangles correspond to the values extrapolated for higher stellar masses.

As an example, Fig. 2 shows two chemical profiles in terms of outer mass fraction at $T_{eff} \approx 80\,000$ K on the cooling curve for a sequence with stellar mass $M_{WD} = 1.019\ M_\odot$ and a C/O core. The bottom panel shows the chemical profile for the He-atmosphere case and the top panel presents the chemical profile for the H-atmosphere sequence, after $M_H = 10^{-5.7} M_{WD}$ of hydrogen was artificially added

Downloaded from https://academic.oup.com/mnras/article-abstract/480/2/1547/5065044 by Universidade Federal do Rio Grande do Sul user on 16 January 2019

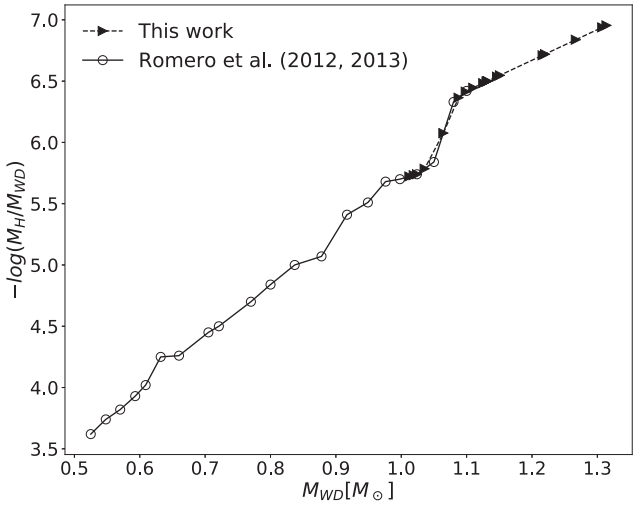


**Figure 1.** Range of star mass and hydrogen envelope mass. Circles are from Romero et al. (2012, 2013) and triangles are the extrapolated data.

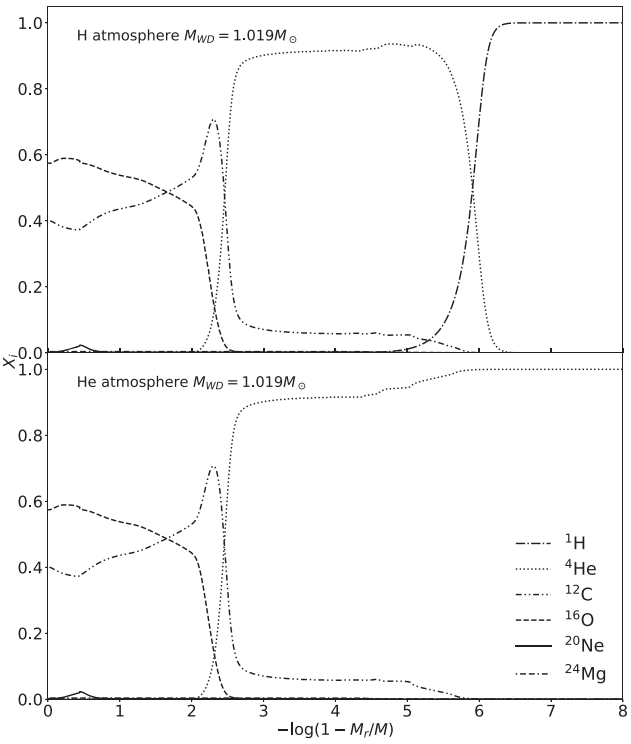


**Figure 2.** Example of chemical profile in terms of the outer mass fraction at $T_{\rm eff} \approx 80\,000$ K on the cooling sequence for H-atmosphere (top) and He-atmosphere (bottom) white dwarfs with 1.019 $M_\odot$. Hydrogen had to be added to all sequences due to losses in the mass-loss phase. The quantities added to each evolution are shown in Table 1. This figure shows that only the atmosphere of the star was changed. The nuclei composition are identical to both H- and He-atmosphere sequences.

to the model. Note that the only difference between the two chemical profiles shown in Fig. 2 is the chemical abundance of the outer layers, while the core regions remain the same.

The sequences with final masses $M_{\rm WD} \geq 1.024$ $M_\odot$ experience loops at high luminosity and at the high effective temperature region in the post-AGB stage (see Fig. 3). The loops are due to carbon shell-burning followed by helium shell-burning, which, for

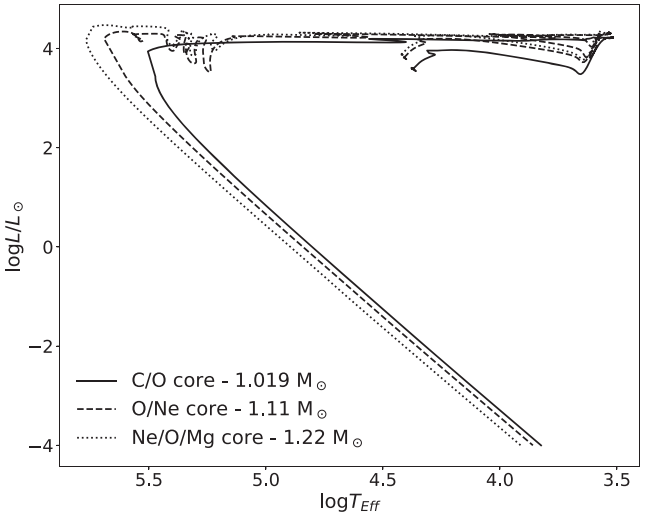


**Figure 3.** Evolutionary tracks for three sequences in the HR diagram, with initial masses 8.9 $M_\odot$ (solid line), 10 $M_\odot$ (dashed line) and 11 $M_\odot$ (dotted line) and final masses 1.019, 1.11 and 1.22 $M_\odot$, respectively. Each sequence has a different core composition in the white dwarf cooling curve stage, which are C/O, O/Ne and Ne/O/Mg for the sequences with white dwarf masses 1.019, 1.11 and 1.22 $M_\odot$, respectively.

sequences with $M_{\rm WD} \geq 1.132$ $M_\odot$, burns all the helium content in the outer layers. This helium shell-burning occurs as a result of the huge temperature gradient on the shells surrounding the core. Thus, enough shells must be added to the numerical models in these regions to account for the large temperature gradients and composition gradients in the shell-burning regions.

For sequences with $M_{\rm WD} \geq 1.132$ $M_\odot$, helium was added on top of the model at the beginning of the cooling sequence using the same procedure used to add hydrogen. The amount of helium to be added was extrapolated from our sequences, which had not burnt all the helium. The amount of hydrogen and helium for each sequence is presented in columns 3 and 4 of Table 1, along with the initial mass at the ZAMS and the white dwarf mass in columns 1 and 2, respectively. Helium-atmosphere sequences were produced by not adding hydrogen on top of the models.

The Hertzsprung–Russell (HR) diagram from the ZAMS to the white dwarf cooling sequence is shown in Fig. 3 for three sequences with initial masses 8.9, 10 and 11 $M_\odot$ and final masses of 1.019, 1.11 and 1.22 $M_\odot$ in the cooling curve, respectively. Each sequence in this figure has a different core composition as a white dwarf star. The solid, dashed and dotted lines represent a C/O core white dwarf with $M_{\rm WD} = 1.019$ $M_\odot$, an O/Ne core white dwarf with $M_{\rm WD} = 1.11$ $M_\odot$ and a Ne/O/Mg white dwarf with $M_{\rm WD} = 1.22$ $M_\odot$, respectively.

The $M_{\rm WD} = 1.019$ $M_\odot$ sequence with a C/O core experienced a core hydrogen-burning stage lasting for 24.51 Myr, and then during the next 2.80 Myr helium was burnt until depletion at the centre. For more massive sequences, the time spent on main-sequence and central helium-burning decreases. For the sequences with final mass $M_{\rm WD} = 1.11$ $M_\odot$, with an O/Ne core, the total main-sequence time is 19.75 Myr plus 2.28 Myr to burn all helium. Lastly, the sequence with final mass $M_{\rm WD} = 1.22$ $M_\odot$ burnt hydrogen for 16.83 Myr until depletion at the centre and burnt helium for 1.81 Myr until extinction at the centre. The ages for hydrogen and helium depletion at centre and progenitor age (i.e. the age at the beginning of the white dwarf cooling sequence) are listed in columns 3, 4 and 5 of Table 3, respectively (see Section 3.6).



Downloaded from https://academic.oup.com/mnras/article-abstract/480/2/1547/5065044 by Universidade Federal do Rio Grande do Sul user on 16 January 2019

**Table 1.** Values of initial mass at ZAMS ($M_{\rm ZAMS}$), white dwarfs masses ($M_{\rm WD}$) and hydrogen content for H-rich sequences and helium content for both H- and He-atmosphere sequences. The H abundances were extrapolated from Romero et al. (2012, 2013). The He abundances were extrapolated for sequences with $M_{\rm WD} \geq 1.132$.

| $M_{\rm ZAMS}$ ($M_\odot$) | $M_{\rm WD}$ ($M_\odot$) | $-\log M_{\rm H}/M_{\rm WD}$ | $-\log M_{\rm He}/M_{\rm WD}$ |
|---|---|---|---|
| 8.80 | 1.012 | 5.722 | 2.451 |
| 8.90 | 1.019 | 5.732 | 2.466 |
| 9.00 | 1.024 | 5.740 | 3.477 |
| 9.20 | 1.036 | 5.785 | 3.349 |
| 9.50 | 1.064 | 6.076 | 2.958 |
| 9.80 | 1.088 | 6.365 | 4.006 |
| 10.00 | 1.110 | 6.446 | 3.517 |
| 10.10 | 1.125 | 6.484 | 2.447 |
| 10.20 | 1.131 | 6.498 | 2.489 |
| 10.30 | 1.132 | 6.500 | 2.495 |
| 10.45 | 1.147 | 6.536 | 2.597 |
| 10.50 | 1.151 | 6.547 | 2.628 |
| 10.80 | 1.216 | 6.711 | 3.089 |
| 11.00 | 1.220 | 6.720 | 3.116 |
| 11.40 | 1.267 | 6.838 | 3.449 |
| 11.80 | 1.307 | 6.939 | 3.735 |

### 3.1 Carbon flame

As can be seen from Fig. 3, the sequences characterized with white dwarf masses of 1.11 and 1.22 $M_\odot$ present loops in the upper-left region of the HR diagram, prior to entering the white dwarf cooling sequence. Those loops are due to carbon-burning, which ignites off-centre and moves inwards to the centre of the star. In particular, towards the end of the loop, just before the extinction of the carbon-burning, helium ignites on a shell near the surface. All sequences with $M_{\rm WD} \geq 1.024$ $M_\odot$ experience an off-centre carbon ignition prior to the white dwarf stage, and for sequences with $M_{\rm WD} \geq 1.132$ $M_\odot$ the subsequent helium-burning consumes all the helium content in the outer layers. If the carbon flame does not reach the centre of the star, a hybrid C/O–O/Ne white dwarf will form (Denissenkov et al. 2013), while if the flame propagates to the centre, an O/Ne/Mg white dwarf will be produced. The occurrence of the late carbon flashes can be an explanation for the luminosity variations observed in the star in the Stingray Nebula, CD-59 6479 or SAO 24567 (Henize 1976; Reindl et al. 2014). The luminosity variation time-scale at the beginning of the carbon-burning in our sequence with $M_{\rm WD} = 1.024$ $M_\odot$ is similar to that observed, although the total change in luminosity in CD-59 6479 is larger than the one shown in our models by a factor of ∼100 (Schaefer & Edwards 2015), and the stellar masses are very different.

All sequences that experienced a carbon flame presented subsequent flames, which started further away from the centre and were quenched before the starting point of the previous flame. Fig. 4 shows the location in mass where the first carbon ignition occurs (solid line) and the location of the extinction of the carbon flame that got closest to the centre (dashed line), as a function of the white dwarf mass that experienced a carbon flame. Note that the sequences with stellar mass $M_{\rm WD} < 1.024$ $M_\odot$ do not experience carbon ignition. The dotted vertical lines separate the mass range for different core compositions (see Section 3.3). As can be seen from this figure, the position of the first carbon ignition becomes closer to the centre of the model for increasing white dwarf mass. As the core mass increases, the central degeneracy is lower, allowing the inner maximum temperature to be near the centre, causing a carbon ignition closer to the centre on more massive sequences.

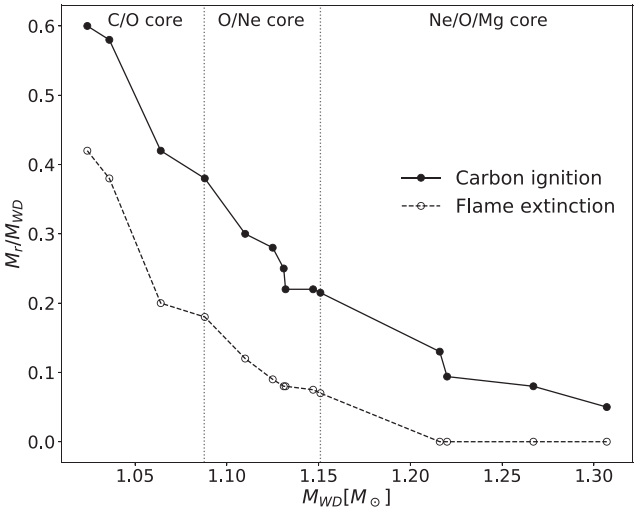


**Figure 4.** Mass location of the first ignition of carbon and mass location of that closest to centre flame extinction as a function of white dwarf masses that experienced a carbon flame. Vertical dotted lines show the limits of the mass range for core composition. See text for details.

Specifically, the sequence with $M_{\rm ZAMS} = 10$ $M_\odot$ ($M_{\rm WD} = 1.11$ $M_\odot$) experiences an off-centre carbon ignition starting at $M_{\rm r}/M_{\rm WD} \sim 0.3$, which moves inwards until $M_{\rm r}/M_{\rm WD} \sim 0.1$, while for the sequence with $M_{\rm ZAMS} = 11.0$ $M_\odot$ ($M_{\rm WD} = 1.220$ $M_\odot$) carbon ignition starts at $M_{\rm r}/M_{\rm WD} \sim 0.094$ and, in this case, reaches the centre of the star. Carbon ignition in all sequences started in regions with density $\rho \sim 1.5 \times 10^6$ g cm$^{-3}$, agreeing with the results for super-AGB sequences from Farmer et al. (2015). For a detailed discussion about carbon-burning, we refer to the works of Siess (2006, 2007) and Farmer et al. (2015), and references therein.

From our computations, some sequences with a C/O core in the white dwarf stages experienced carbon ignition, but the carbon flame only reached $M_{\rm r}/M_{\rm WD} \sim 0.2$ for those models. When the carbon flame reaches the regions closer than $M_{\rm r}/M_{\rm WD} < 0.2$, a hybrid C/O–O/Ne white dwarf with an O/Ne core is formed. For sequences with $M_{\rm WD} > 1.15$ $M_\odot$, the carbon flame reaches the



Downloaded from https://academic.oup.com/mnras/article-abstract/480/2/1547/5065044 by Universidade Federal do Rio Grande do Sul user on 16 January 2019

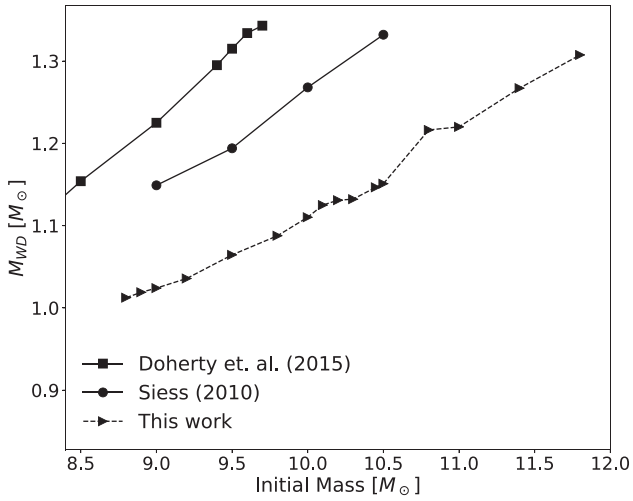


**Figure 5.** Initial-to-final mass relation obtained from our computations (triangles) compared with the results from Siess (2010) and Doherty et al. (2015), shown as circles and squares, respectively. In all cases, the initial metallicity is $Z = 0.02$. We only show the massive models of Doherty et al. (2015).

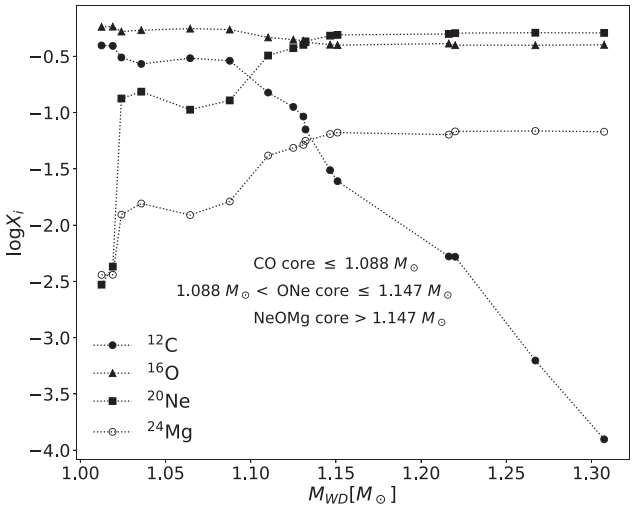


**Figure 6.** Central abundances versus final mass of the white dwarf stars before crystallization starts ($T_{\rm eff} \approx 40\,000$ K). The black circles represent $^{12}$C, triangles are $^{16}$O, squares are $^{20}$Ne and empty circles are $^{24}$Mg. We can identify three regions: one for a C/O core for masses below or equal to 1.088 $M_\odot$ where neon is lower than carbon; another region between 1.088 and 1.147 $M_\odot$ in which neon is greater than carbon and lower than oxygen but magnesium is lower than carbon, defining an O/Ne core; and a third region for masses greater than 1.147 $M_\odot$ with an O/Ne/Mg core due to neon being greater than oxygen and magnesium greater than carbon.

centre of the star, producing a Ne/O/Mg core white dwarf. The details of core composition and chemical profile will be analysed in the following subsections.

### 3.2 The initial-to-final mass relation

Fig. 5 presents the initial-to-final mass relation obtained from our computations, compared with the results of Siess (2010) and Doherty et al. (2015), within the stellar mass range considered in this work. We consider models with metallicity $Z = 0.02$. The final mass obtained in this work is systematically lower than previous results, because of the different input physics considered in each case. Siess (2010) considers the Vassiliadis & Wood (1993) mass-loss scheme, a mixing-length parameter of $\alpha_{\rm MLT} = 1.75$ and no core overshooting. However, Doherty et al. (2015) consider the mass-loss rate from Reimers (1975) on the RGB, followed by Bloecker (1995) at high luminosities and changing to Vassiliadis & Wood (1993) in the thermally pulsing phase, with a similar convection treatment as Siess (2010). Also, both Siess (2010) and Doherty et al. (2015) evolved their sequences only until the TP-AGB phase, and then considered the mass of the He-free core as the final mass at the white dwarf stage. As discussed in Siess (2010), the final mass is dependent on the core growth and mass-loss scheme. In our computations, we calculated full evolutionary sequences by employing the mass-loss formula from Reimers (1975) on the RGB and from Bloecker (1995) on the AGB, with a larger efficiency parameter than the mass-loss rates considered by previous authors. Thus, the sequences evolve to the post-AGB phase and lead to a lower final mass in the cooling curve for the same initial mass. From our computations, the upper limit of progenitor mass needed to produce a white dwarf star is $M_{ZAMS} = 11.8$ $M_\odot$ for $Z = 0.02$, which is 21.6 % greater than the value found by Doherty et al. (2015) and 12.4 % greater compared with Siess (2010) for the same initial metallicity. Considering the dispersion in the initial-to final mass relation from the different authors in Fig. 5, for a given initial mass in the ZAMS we can estimate a range of final white dwarf masses. For instance, a sequence with an initial mass of 9 $M_\odot$ can produce a white dwarf with masses ranging from 1.024 to 1.225 $M_\odot$, depending on the input physics applied, especially the mass-loss formulation. The present-day observational data cannot distinguish the best model.

### 3.3 Central abundances in the cooling sequence

Within the stellar mass range studied in this work, we expect to have three main core compositions – that is, C/O and O/Ne (García-Berro, Ritossa & Iben 1997b; Doherty et al. 2015) or Ne/O/Mg, changing with increasing stellar mass. Fig. 6 shows central abundances of carbon, oxygen, neon and magnesium in a logarithmic scale, as a function of the white dwarf mass. The values are taken at $T_{\rm eff} \approx 40\,000$ K, an effective temperature low enough to give time for diffusion to act on the central composition and still high enough to be above crystallization. As shown in Fig. 6, the C/O core is dominant for $M_{\rm WD} \leq 1.088$ $M_\odot$ due to carbon being more abundant than neon. In the range $1.088 < M_{\rm WD} \leq 1.147$ $M_\odot$, we have an O/Ne core as the amount of neon increases but is still lower than oxygen, whilst for masses $M_{\rm WD} > 1.147$ $M_\odot$ neon is the most abundant element in the central composition, followed by oxygen and then by magnesium, defining the core composition as a Ne/O/Mg core. Note that sequences with $M_{\rm WD} > 1.15$ $M_\odot$ experienced a carbon flame that reaches the centre of the stars, as shown in Fig. 4 and discussed in Section 3.1. Also, the sequence with $M_{\rm WD} = 1.024$ $M_\odot$ is the sequence with the lowest stellar mass to experience carbon-burning, but it does not reach the centre, producing a hybrid C/O–O/Ne white dwarf. This explains the step in the central $^{20}$Ne abundance observed in Fig. 6 for that stellar mass. Doherty et al. (2015) computed sequences for super-AGB stars and found that, for $Z = 0.02$, sequences with core masses $M_{\rm c} < 1.075$ $M_\odot$ become a C/O core white dwarf, sequences with core masses $1.075 \leq M_{\rm c} < 1.154$ $M_\odot$ present a C/O/Ne core, and for core masses $M_{\rm c} \geq 1.154$ $M_\odot$ the sequences are O/Ne white dwarfs. Woosley & Heger (2015) also calculated sequences on the limit of supernova progenitors and obtained models with an O/Ne core for a



Downloaded from https://academic.oup.com/mnras/article-abstract/480/2/1547/5065044 by Universidade Federal do Rio Grande do Sul user on 16 January 2019

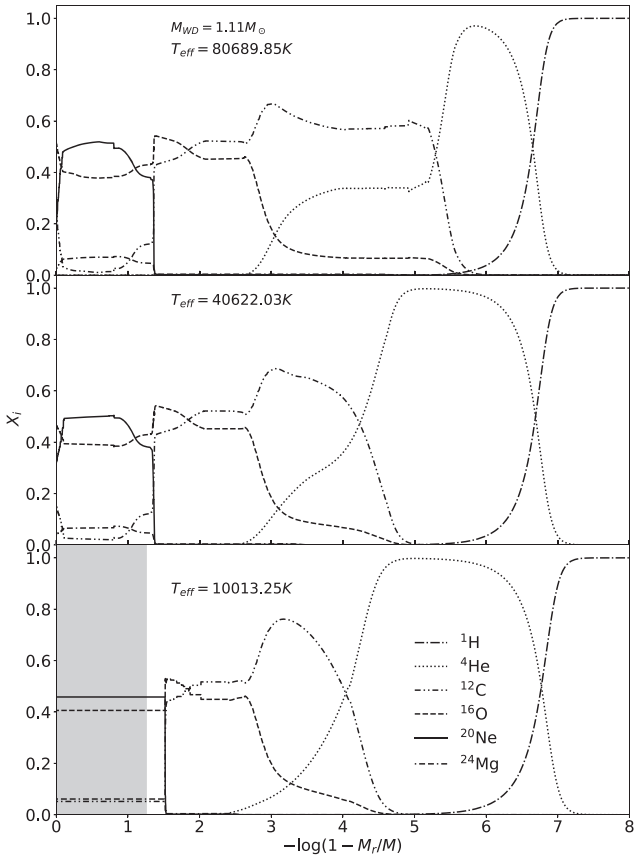


**Figure 7.** Chemical profile in terms of outer mass fraction for selected elements for three different stages of the cooling sequence: $T_{\rm eff} \approx 80\,000$ K (top panel), $T_{\rm eff} \approx 40\,000$ K (middle) and $T_{\rm eff} \approx 10\,000$ K (bottom). The chemical profiles are for a H-atmosphere white dwarf with $M_{\rm WD} = 1.11$ M$_\odot$. The shaded region represents the crystallized zone of the star.

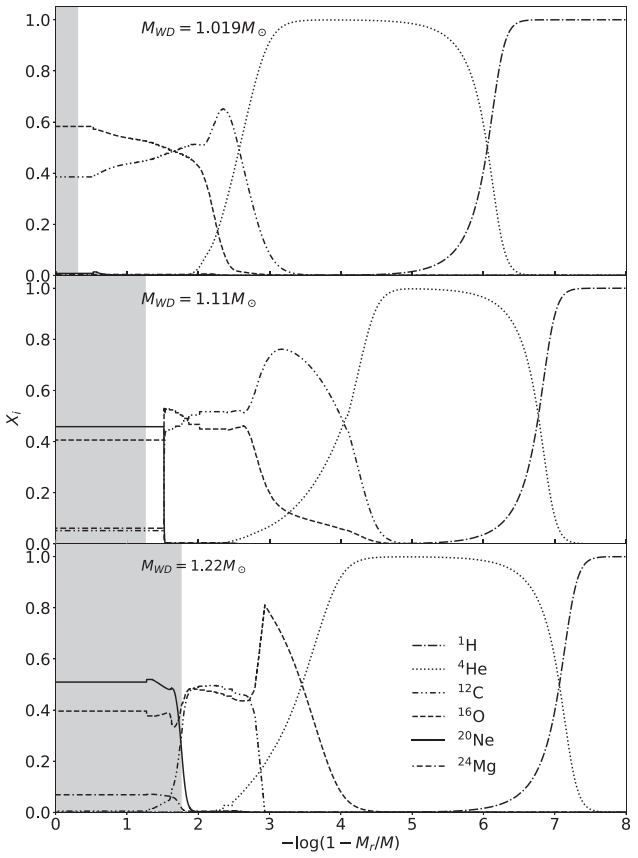


**Figure 8.** Chemical profile in terms of outer mass fraction for selected elements and for three different H-atmosphere white dwarfs with $T_{\rm eff} \approx 10\,000$ K. From top to bottom, we depict the chemical profiles for $M_{\rm WD} = 1.019$, 1.11 and 1.22 M$_\odot$. The shaded region represents the crystallized zone of the star.

range of core mass $1.088 \leq M_{\rm c} \leq 1.345$ M$_\odot$. Chemical profiles from Doherty et al. (2015) and Woosley & Heger (2015) are not publicly available so we cannot compare the internal abundances of the last models computed. It is important to note that Doherty et al. (2015) and Woosley & Heger (2015) did not compute the cooling curves, in contrast to the present work. They also use different evolutionary codes with different nuclear reactions and input physics.

### 3.4 Chemical profiles in the white dwarf cooling sequence

In Fig. 7, we show three chemical profiles for models along the white dwarf cooling sequence for an O/Ne core H-atmosphere white dwarf with stellar mass $M_{\rm WD} = 1.11$ M$_\odot$. The abundance profiles are in terms of outer mass fraction and correspond to three effective temperatures, $T_{\rm eff} \approx 80\,000$, 40 000 and 10 000 K, in the top, middle and bottom panels, respectively. The effects of diffusion and gravitational settling on the entire chemical profile as the star cools are evident from this figure. Initially, the oxygen central abundance is $X_{\rm O} = 0.515$ while for neon it is $X_{\rm Ne} = 0.195$ (top panel). Rehomogenization processes change the central abundances to a flat profile with $X_{\rm O} = 0.406$ and $X_{\rm Ne} = 0.458$ when the star reaches effective temperatures $\sim$10 000 K (bottom panel). Also, there is a carbon–oxygen–helium triple-layer structure at $2.7 < -\log(1 - M_{\rm r}/M) < 5.5$ for high effective temperatures, which diminishes due to diffusion processes. Note that, for the sequence with white dwarf mass 1.11 M$_\odot$, the carbon flame experienced in the pre-white-dwarf stages, did not reach the centre of the model, giving rise to white dwarfs with a hybrid C/O–O/Ne core (Denissenkov et al. 2013; Doherty et al. 2015; Farmer et al. 2015). The hybrid models presented in Denissenkov et al. (2013) are characterized by a C/O core surrounded by an O/Ne region at the super-AGB stage. This chemical structure differs from the one characterizing our models (see Fig. 7), as ours is taken from the white dwarf cooling curve, where rehomogenization processes are taken into account. To our knowledge, this is the first time a chemical profile for the entire star is presented for a hybrid C/O–O/Ne white dwarf. The shaded region in the bottom panel depicts the crystallized core, which is defined as the region where $\Gamma \geq 220$ (see Section 3.5). For this sequence, crystallization starts at $T_{\rm eff} \approx 20\,000$ K. Finally, the chemical structure of the star can be separated into the outer layers, composed by hydrogen followed by an extended helium buffer, and the inner regions show a triple layer of carbon–oxygen–helium from $2 < -\log(1 - M_{\rm r}/M) < 4$ with a carbon peak ($-\log M_{\rm r}/M \sim 3.1$) on top of the Ne/O core. This chemical structure of the core is the result of burning events occurring in previous stages to the white dwarf cooling sequence.

The composition of the core and its size have a strong impact on the chemical profile of the entire star. Fig. 8 shows the chemical profiles in terms of outer mass fraction for three H-atmosphere white dwarf models with $T_{\rm eff} \approx 10\,000$ K, with stellar mass $M_{\rm WD} = 1.019$ M$_\odot$ (top panel), $M_{\rm WD} = 1.11$ M$_\odot$ (middle panel) and

Downloaded from https://academic.oup.com/mnras/article-abstract/480/2/1547/5065044 by Universidade Federal do Rio Grande do Sul user on 16 January 2019

**Table 2.** Age and effective temperature on the onset of crystallization for different Coulomb coupling parameters. The age of crystallization is defined as the time starting at the cooling sequence and ending at the onset of crystallization (given in Gyr). The effective temperature is in Kelvin. The effective temperature for $\Gamma_{\rm full} = 220$ in the last row agrees with table 2 of Romero et al. (2013).

| $M_{\rm WD}$ ($M_\odot$) | $\Gamma_{\rm full} = 175$ | | $\Gamma_{\rm full} = 220$ | |
|---|---|---|---|---|
| | Age (Gyr) | $T_{\rm eff}$ (K) | Age (Gyr) | $T_{\rm eff}$ (K) |
| 1.012 | 15095 | 0.647 | 13152 | 0.871 |
| 1.019 | 15376 | 0.628 | 13396 | 0.848 |
| 1.024 | 15552 | 0.678 | 13584 | 0.925 |

$M_{\rm WD} = 1.22$ $M_\odot$ (bottom panel). The shaded region represents the crystallized region of the model. From this figure, we note that the crystallization front is closer to the surface of the model for higher stellar mass, located at $-\log(1 - M_r/M) \approx 0.9$, 1.2 and 2 for $M_{\rm WD} = 1.019$, 1.11 and 1.22 $M_\odot$ models, respectively. The sequence characterized by stellar mass $M_{\rm WD} = 1.019$ $M_\odot$ has a C/O core with a core mass of $M_c = 1.016$ $M_\odot$ extending to $-\log(1 - M_r/M_*) = 2.6$ and present a triple layer of carbon–oxygen–helium at $1.8 < -\log(1 - M_r/M_*) < 2.6$. On top of the core, the model has a helium buffer of $M_{\rm He} = 10^{-2.47} M_{\rm WD}$ and a hydrogen envelope with $M_{\rm H} = 10^{-5.73} M_{\rm WD}$. All these structures have a strong impact on the propagation of stellar oscillations, when present (Winget et al. 1997). Althaus et al. (2010) and Romero et al. (2012, 2013) also obtained a triple-layer structure in their C/O core white dwarf models.

The sequence with $M_{\rm WD} = 1.11$ $M_\odot$ has an O/Ne core, extending to $-\log(1 - M_r/M) = 4$, which represents mass $M_c = 1.1099$ $M_\odot$. As discussed before, this O/Ne core model shows a triple-layer oxygen–carbon–helium with a peak of carbon at the outer boundary of the core, a helium buffer of $M_{\rm He} = 10^{-3.52} M_{\rm WD}$ and a hydrogen envelope of $M_{\rm H} = 10^{-6.45} M_{\rm WD}$. The $M_{\rm WD} = 1.22$ $M_\odot$ sequence has a Ne/O/Mg core with $M_c = 1.219$ $M_\odot$, which extends to $-\log(1 - M_r/M) = 3.5$. It also presents a triple layer of oxygen–carbon–helium with a sharp oxygen peak, instead of a carbon peak in the O/Ne core case. The Ne/O/Mg core model has a helium buffer of $M_{\rm He} = 10^{-3.12} M_{\rm WD}$ and a hydrogen envelope of $M_{\rm H} = 10^{-6.72} M_{\rm WD}$. The differences in core composition are due to the final mass, as shown in Fig. 6. Asteroseismology will be able to distinguish these structures.

In the Appendix, we present all chemical profiles for both H- and He-atmosphere sequences at effective temperatures $T_{\rm eff} \approx 10\,000$ K.

### 3.5 Crystallization and the Coulomb coupling parameter

As stated before, as a standard input value the MESA code considers that a mixture of solid and liquid phases occurs for a coupling parameter $\Gamma_i = 150$ while a full crystal structure occurs when $\Gamma_{\rm full} = 175$. However, Romero et al. (2013) calculated white dwarf sequences considering two types of phase diagram. They concluded that the azeotropic type from Horowitz et al. (2010) better represents the crystallization on the nuclei of white dwarfs. Hence, we modify the values of the $\Gamma$ parameter to $\Gamma_i = 215$ for a liquid/solid coexisting phase and $\Gamma_{\rm full} = 220$ for a full crystal phase, in line with the results obtained using the Horowitz et al. (2010) phase diagram. Paxton et al. (2018) calculated cooling sequences for a 0.6-$M_\odot$ white dwarf star, using MESA, varying $\Gamma_i = 174 - 220$ and $\Gamma_{\rm full} = 176 - 240$, and they found a difference in the cooling times of the order of ∼0.2 Gyr. For the stellar mass range considered in this work, an assumption of $\Gamma_i = 215$ and $\Gamma_{\rm full} = 220$ makes the effective temperature at which crystallization starts ≈2000 K lower, and the age ≈0.23 Gyr larger than the values using the standard input values. Table 2 lists the effective temperature and age on the onset of crystallization for three sequences considering the two values of $\Gamma_{\rm full}$ .

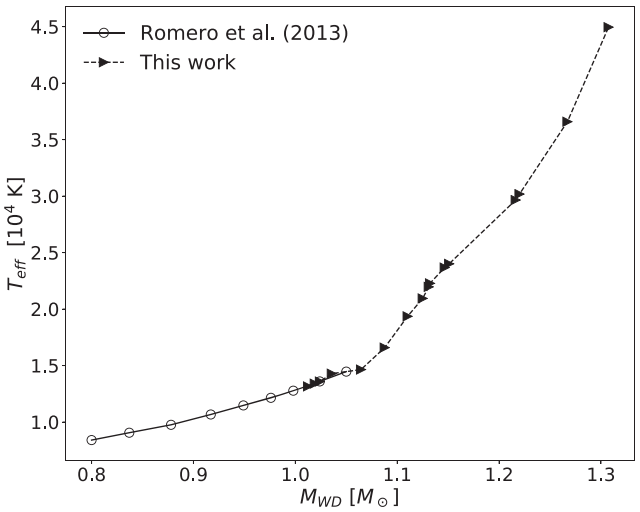


**Figure 9.** Comparison of effective temperature on the onset of crystallization for a range of white dwarf masses. Effective temperature is in units of $10^4$ K. Circles denote the data extracted from Romero et al. (2013) and triangles are results from this work. There is agreement between both works for values of mass $M_{\rm WD} \sim 1$ $M_\odot$ and the effective temperature rises as mass also increases.

In Fig. 9, we compare the values of the effective temperature at the onset of crystallization, as a function of the white dwarf mass, with the results obtained by Romero et al. (2013). Note that the results obtained in this work (shown by triangles) are in good agreement with those from Romero et al. (2013), shown by circles, in the stellar mass range where both works overlap.

### 3.6 White dwarf cooling times

The cooling time is defined as the time spent by a star in the white dwarf cooling sequence ($t_{\rm cool}$). We define the beginning of the cooling sequence as the point of maximum effective temperature in the post-AGB stage, before the star enters the cooling sequence. The progenitor age ($t_i$) is defined as the time from the ZAMS to the beginning of the cooling sequence. Then the total age of a white dwarf star can be computed as $t_{\rm total} = t_i + t_{\rm cool}$. Table 3 summarizes the characteristic time-scales for all the sequences computed in this work. Specifically, for each sequence, we list the initial mass in the ZAMS (column 1) and the final mass at the cooling curve (column 2), along with the age for hydrogen and helium exhaustion at the core in columns 3 and 4, respectively. The progenitor age $t_i$



Downloaded from https://academic.oup.com/mnras/article-abstract/480/2/1547/5065044 by Universidade Federal do Rio Grande do Sul user on 16 January 2019

**Table 3.** Mass at ZAMS, white dwarf mass, age when hydrogen is depleted at centre ($t_H$), age when helium is totally consumed at the centre ($t_{He}$), progenitor ages ($t_i$), effective temperature on crystallization ($T_{eff_c}$) and age at crystallization ($t_{cryst}$, accounted from the beginning of the cooling sequence) and cooling time ($t_{cool}$ = age at $T_{eff} = 1 \times 10^4$ K minus $t_i$) for H- and He-atmosphere white dwarfs. Ages ($t_H$, $t_{He}$, $t_i$) in units of Myr and crystallization and cooling times in units of Gyr.

| | | | | | H-atmosphere | | | He-atmosphere | | |
|---|---|---|---|---|---|---|---|---|---|---|
| $M_{ZAMS}$ ($M_\odot$) | $M_{WD}$ ($M_\odot$) | $t_H$ (Myr) | $t_{He}$ (Myr) | $t_i$ (Myr) | $T_{eff_c}$ (K) | $t_{cryst}$ (Gyr) | $t_{cool}$ (Gyr) | $T_{eff_c}$ (K) | $t_{cryst}$ (Gyr) | $t_{cool}$ (Gyr) |
| 8.80 | 1.012 | 24.99 | 27.87 | 28.53 | 13 152 | 0.870 | 3.65 | 13 738 | 0.839 | 2.99 |
| 8.90 | 1.019 | 24.50 | 27.30 | 27.94 | 13 396 | 0.847 | 3.69 | 13 837 | 0.839 | 2.99 |
| 9.00 | 1.024 | 23.88 | 26.61 | 27.26 | 13 584 | 0.924 | 4.09 | 13 634 | 0.933 | 3.48 |
| 9.20 | 1.036 | 22.99 | 25.73 | 26.24 | 14 281 | 0.810 | 3.75 | 14 714 | 0.756 | 3.36 |
| 9.50 | 1.064 | 21.63 | 24.17 | 24.63 | 14 643 | 0.754 | 3.13 | 14 098 | 0.924 | 2.85 |
| 9.80 | 1.088 | 20.49 | 22.82 | 23.24 | 16 585 | 0.636 | 3.39 | 15 858 | 0.742 | 2.90 |
| 10.00 | 1.11 | 19.75 | 22.03 | 22.45 | 19 356 | 0.415 | 3.04 | 17 945 | 0.538 | 2.62 |
| 10.10 | 1.125 | 19.42 | 21.64 | 22.03 | 20 941 | 0.338 | 2.65 | 19 552 | 0.405 | 2.34 |
| 10.20 | 1.131 | 19.06 | 21.23 | 21.62 | 21 963 | 0.310 | 2.72 | 19 815 | 0.387 | 2.48 |
| 10.30 | 1.132 | 18.75 | 20.87 | 21.26 | 22 276 | 0.296 | 2.71 | 20 383 | 0.376 | 2.57 |
| 10.45 | 1.147 | 18.35 | 20.37 | 20.74 | 23 673 | 0.253 | 2.52 | 23 006 | 0.285 | 2.21 |
| 10.50 | 1.151 | 18.19 | 20.17 | 20.54 | 24 001 | 0.250 | 2.51 | 23 339 | 0.278 | 2.21 |
| 10.80 | 1.216 | 17.38 | 19.31 | 19.55 | 29 651 | 0.183 | 2.28 | 29 982 | 0.181 | 1.91 |
| 11.00 | 1.22 | 16.83 | 18.63 | 18.88 | 30 177 | 0.177 | 2.25 | 30 244 | 0.179 | 1.90 |
| 11.40 | 1.267 | 15.86 | 17.51 | 17.73 | 36 584 | 0.133 | 1.93 | 36 808 | 0.132 | 1.71 |
| 11.80 | 1.307 | 15.02 | 16.55 | 16.75 | 44 953 | 0.098 | 1.54 | 45 137 | 0.099 | 1.31 |

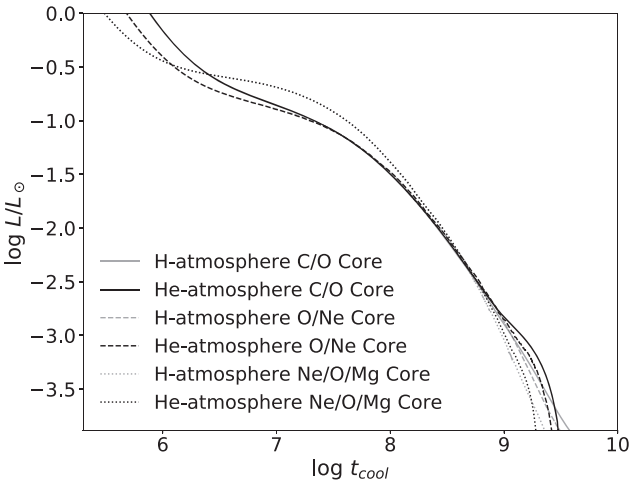


**Figure 10.** Cooling times for selected H- and He-atmosphere cooling sequences. We present three sets of H- and He-atmosphere sequences: a C/O core set with mass 1.019 $M_\odot$ (solid line), an O/Ne set with mass 1.11 $M_\odot$ (dashed line) and a Ne/O/Mg set with mass 1.22 $M_\odot$ (dotted line). Grey and black lines represent H-atmosphere and He-atmosphere white dwarf sequences, respectively. The final chemical profile for the H-atmosphere sequences are shown in Fig. 8.

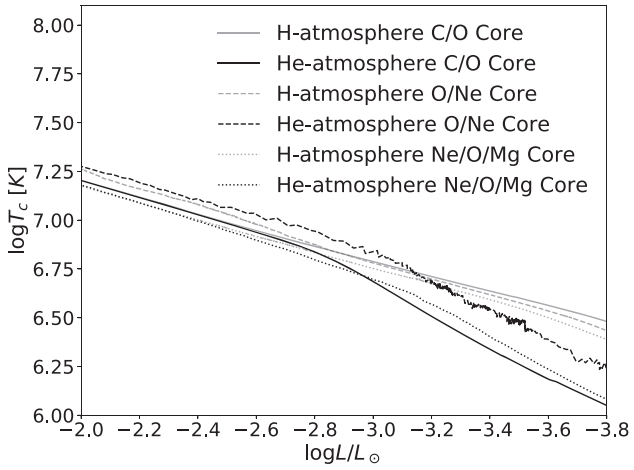


**Figure 11.** Logarithm of central temperature in terms of star luminosity. Three sets of H- and He-atmosphere white dwarfs are shown, the same as in Fig. 10. Faint and strong lines represent H-atmosphere and He-atmosphere white dwarfs, respectively.

is listed in column 5. The age for hydrogen and helium depletion and the progenitor age are equal for both H- and He-atmosphere white dwarf sequences, as both have evolved equally in the stages prior to the cooling sequence. We also list the effective temperature and the age in the cooling curve at the onset of crystallization for the H-atmosphere (columns 6 and 7) and He-atmosphere (columns 9 and 10) sequences. Finally, the cooling times corresponding to an effective temperature of 10 000 K are listed in columns 8 and 12 for sequences with hydrogen and helium atmospheres, respectively.

Figure 10 shows the cooling times for H- and He-atmosphere sequences with the same stellar mass, 1.019 (solid line), 1.11 (dashed line) and 1.22 $M_\odot$ (dotted line), whose chemical profiles are presented in Fig. 8. Grey lines represent H-atmosphere sequences and black lines correspond to He-atmosphere sequences. For luminosities log $L/L_\odot \gtrsim -2.8$, He-atmosphere sequences cool more slowly than their H-atmosphere counterparts. However, for log $L/L_\odot \lesssim -2.8$, He-atmosphere sequences cool considerably faster, leading to differences in the cooling age of $\sim$1 Gyr for luminosities of log $L/L_\odot \sim -4$. This behaviour can be explained by means of the central temperature of the star. Fig. 11 depicts the central temperature $T_c$, in a logarithmic scale, in terms of the surface luminosity for the sequences presented in Fig. 10.

For luminosities higher than log $L/L_\odot \approx -3$, the central temperature for the He-atmosphere sequences is slightly larger than in the case of a H-atmosphere sequence with the same mass. However, for lower luminosities there is a large difference in



Downloaded from https://academic.oup.com/mnras/article-abstract/480/2/1547/5065044 by Universidade Federal do Rio Grande do Sul user on 16 January 2019

$T_c$ between H- and He-atmosphere sequences. The release of internal energy due to crystallization occurs at higher luminosities for He-atmosphere sequences, delaying the cooling for those luminosities. As helium is more transparent than hydrogen, He-atmosphere sequences lose energy faster than H-atmosphere sequences at lower luminosities. The results presented in Fig. 10 agree with the results from Camisassa et al. (2017, their figs 7 and 11), who calculated evolutionary sequences for lower-mass white dwarfs ($M_{WD} \leq 1$ M$_\odot$) with hydrogen-deficient atmospheres, and compared these with hydrogen-rich white dwarfs from Camisassa et al. (2016).

The core composition also affects the cooling times of white dwarf stars. García-Berro et al. (1997a) compared cooling times for sequences with same mass and two core compositions, C/O and O/Ne , and obtained a difference in cooling time of the order of ∼2 Gyr. This is due to the difference in the heat capacity of the core, which is lower for an O/Ne mixture than for an C/O mixture, reducing the cooling time for a core with a higher mean molecular weight.

The Debye regime of fast cooling for white dwarfs is important for very low luminosities. In particular, Althaus et al. (2007) found that the Debye cooling regime for H-atmosphere white dwarfs starts to be important for luminosities below log$L/L_\odot \sim -4$ for masses $M_{WD} \geq 1.28$ M$_\odot$. Since our computations end at those luminosities, the cooling times presented in Fig. 10 are not affected by Debye cooling.

In the region of $0 > \log L/L_\odot > -1.5$, the effects of neutrino losses are present and dominant, as can be seen from Fig. 10. The neutrino emission decreases at higher luminosities for the more massive sequences when compared to lower-mass sequences, but there are no differences between the H- and He-atmosphere sequences at those luminosities. The rate of neutrino emission becomes negligible at log $L/L_\odot \sim -1$ for the sequences with masses 1.019 and 1.11 M$_\odot$, and at log $L/L_\odot \sim -0.5$ for the sequence with 1.22 M$_\odot$, in agreement with the results from Althaus et al. (2007). However, the evolution for luminosities lower than log $L/L_\odot \sim -2$ in our computations differs from the luminosities computed by Althaus et al. (2007). In our computations, we consider a crystallization treatment that mimics the results from the phase diagram presented by Horowitz et al. (2010), while Althaus et al. (2007) consider the phase diagram from Segretain et al. (1994), which increases the crystallization temperature by ∼2000 K (for details, see Romero et al. 2013). Also, Althaus et al. (2007) consider a fixed O/Ne core chemical profile for all stellar masses, while in the cooling sequences calculated in this work, the chemical profiles come from evolutionary computations and are consistent with the stellar mass, covering C/O, O/Ne and Ne/O/Mg cores. The differences in the cooling times between our computations and those from Althaus et al. (2007) are ∼0.6 Gyr at log$L/L_\odot \sim -4$ for a stellar mass of ∼ 1.21 M$_\odot$.

## 4 MASS–RADIUS RELATION

Fig. 12 shows the mass–radius relation of our sequences with H and He atmospheres, as solid and dashed lines, respectively. We consider effective temperatures of 150 000, 100 000, 50 000, 25 000 and 10 000 K, shown from top to bottom. The rate of contraction is higher for high effective temperatures compared to low effective temperatures. Because of their higher surface gravity, more massive sequences show a smaller range in the value of the radius for the different effective temperatures considered here. For a sequence with the H atmosphere characterized by a stellar mass of 1.267 M$_\odot$, the total radius changes from $4.83 \times 10^{-3}$ R$_\odot$ to $4.34 \times 10^{-3}$ R$_\odot$ when the star cools from 150 000 to 10 000 K. For a sequence with a mass of 1.064 M$_\odot$, the radius decreases from $8.31 \times 10^{-3}$ R$_\odot$ to $6.95 \times 10^{-3}$ R$_\odot$ for the same range of effective temperatures. This means that there is a change in radius of ∼10 % for the more massive sequence and ∼16 % for the latter. These values change when sequences with a He atmosphere are considered. For a He-atmosphere sequence with 1.267 M$_\odot$, the radius change from $4.74 \times 10^{-3}$ R$_\odot$ to $4.32 \times 10^{-3}$ R$_\odot$ (∼9 %), and for the 1.064 M$_\odot$ sequence, there is a change from $8.02 \times 10^{-3}$ R$_\odot$ to $6.90 \times 10^{-3}$ (∼14 %) when considering the same effective temperature range. Note that, although the contraction of H-atmosphere sequences are slightly higher, their final radii are higher compared to their He-atmosphere counterparts, showing that a small amount of hydrogen of the order of $M_H \approx 10^{-6}$ M$_{WD}$ can change the radius by $5.4 \times 10^{-5}$ R$_\odot$ (∼1 %) for an $M_{WD} = 1.064$ M$_\odot$ sequence.

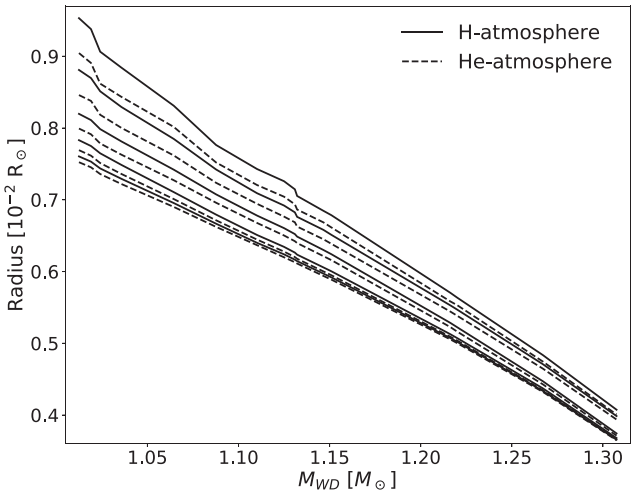


**Figure 12.** Mass–radius relation for H- and He-atmosphere white dwarf models, represented as solid and dashed lines, respectively. From top to bottom, the lines represent effective temperatures of 150 000, 100 000, 50 000, 25 000 and 10 000 K. See text for details.

The surface gravity log $g$ as a function of effective temperature $T_{eff}$ for H- and He-atmosphere sequences are presented in Figs 13 and 14, respectively. The solid lines correspond to C/O core sequences while dashed and dotted lines correspond to O/Ne and Ne/O/Mg core sequences, respectively. Stellar mass decreases from top to bottom. Also plotted, as empty circles, are a selection of white dwarfs with spectroscopic masses $M_{WD} > 1$ M$_\odot$ from the SDSS Data Release (DR) 12 catalogue presented by Kepler et al. (2016). Surface gravities and effective temperatures for H-atmosphere white dwarfs are corrected to 3D convection (Tremblay et al. 2013) and have mean values of $\langle \log g \rangle = 8.987 \pm 0.21$ and $\langle T_{eff} \rangle = 11\,591 \pm 501$. From Fig. 13, we find good agreement between observations and our theoretical cooling sequences with masses $M_{WD} \leq 1.151$ M$_\odot$. Comparing Figs 13 and 14, we can see that the sequences are slightly shifted to smaller gravities, on average $\Delta \log g = 0.0135$, for lower effective temperatures due to contraction, which reduced the radius by $\Delta R = 3.246 \times 10^{-5}$ R$_\odot$ on average. The increase in log $g$ at log $T_{eff} \sim 4.8$–4.9 presented in Figs 13 and 14 for the Ne/O/Mg sequences with $M_{WD} > 1.2$ M$_\odot$ is due to the decrease in the neutrino luminosity, which causes a reduction in the radius of the model. This behaviour agrees with the results from Althaus et al. (2005b) who were the first to report this phenomenon.



Downloaded from https://academic.oup.com/mnras/article-abstract/480/2/1547/5065044 by Universidade Federal do Rio Grande do Sul user on 16 January 2019

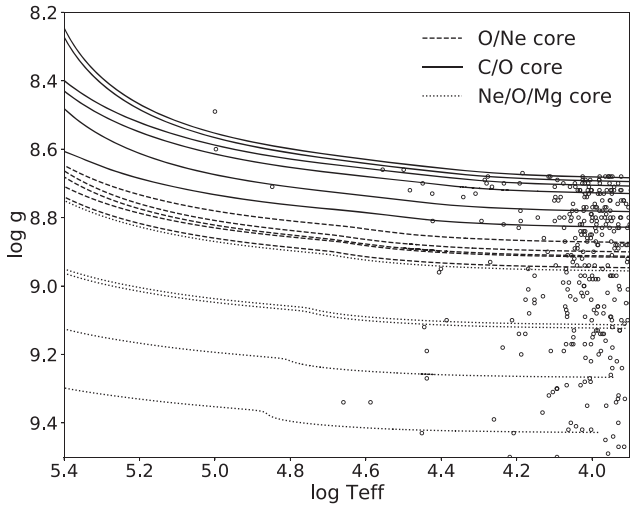


**Figure 13.** The log$g$–$T_{\rm eff}$ relation for H-atmosphere white dwarfs, with $T_{\rm eff}$ from ≈ 250 000 to ≈ 10 000 K. Empty circles correspond to H-atmosphere white dwarf stars from the SDSS catalogue presented in Kepler et al. (2016). See text for details.

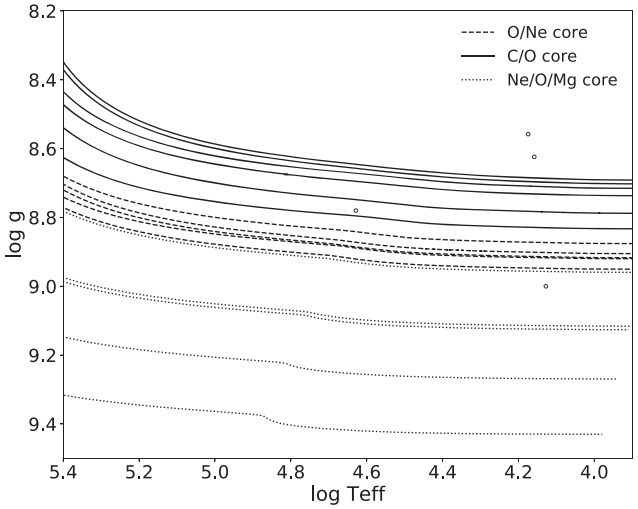


**Figure 14.** The log$g$–$T_{\rm eff}$ relation for He-atmosphere white dwarfs, with $T_{\rm eff}$ from ≈ 250 000 to ≈ 10 000 K. Empty circles correspond to He-atmosphere white dwarf stars from the SDSS catalogue presented in Kepler et al. (2016). See text for details.

For comparison proposes, we compute the stellar mass of a sample of 252 stars from the SDSS DR12 catalogue of Kepler et al. (2016) using the cooling sequence computed in this work and those obtained using the LPCODE evolutionary code (Althaus et al. 2005a; Romero et al. 2013). The results are shown in Fig. 15 where we depict the stellar mass obtained from the MESA tracks against the mass computed using the LPCODE tracks. As can be seen, there is practically no difference between the two determinations. The deviations from the 1 : 1 correspondence for stellar masses around 1.05 $M_\odot$ are due to the transition from a C/O to an O/Ne core composition, which occurs at 1.05 $M_\odot$ for LPCODE, while in our simulations it occurs at 1.088 $M_\odot$.

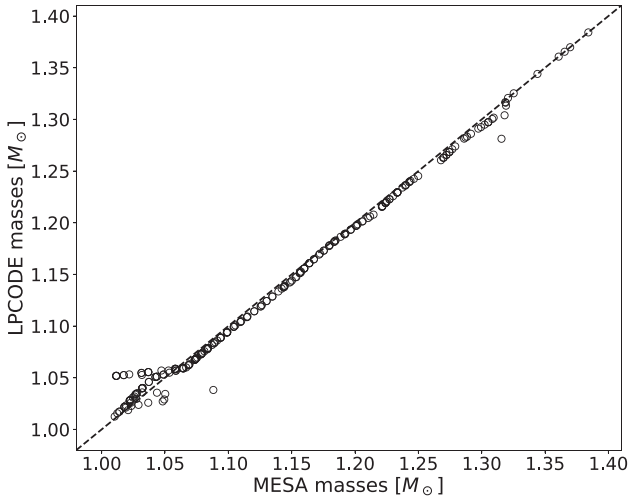


**Figure 15.** Comparison between the stellar mass for a sample of 252 spectroscopically identified DA white dwarf stars from the SDSS DR12 catalogue, computed using the MESA sequences ($x$-axis) and LPCODE sequences ($y$-axis). The dashed line indicates the 1 : 1 correspondence.

## 5 CONCLUSION

In this work, we have calculated full evolutionary sequences with $Z = 0.02$ for massive H- and He-atmosphere white dwarf stars using the evolutionary code MESA version r8845. Our sequences started from the ZAMS with masses from 8.8 to 11.8 $M_\odot$, evolving through central hydrogen- and helium-burning, thermally pulsing and mass-loss phases, ending as white dwarfs on the cooling sequence. The resulting white dwarf sequences show stellar masses in the range of $M_{\rm WD}$ = 1.012–1.307 $M_\odot$. We have presented full chemical profiles, core mass ranges, cooling times with crystallization effects, mass–radius relation and initial-to-final mass relation. We have also calculated masses from our evolutionary tracks for a selection of 252 massive stars from the SDSS DR12 catalogue (Kepler et al. 2016) and compared these with derived masses from other evolutionary tracks presented in the literature.

Unlike models that only evolve to the AGB, our white dwarf sequences consider the entire evolutionary history of the corresponding progenitors, leading to realistic chemical profiles that are also consistent with stellar mass. Note that the amount of hydrogen and helium affects both the age and mass determinations of DA and non-DA white dwarfs. The final mass ranges of our sequences cover the entire range of C/O, O/Ne and Ne/O/Mg core compositions and also account for hybrid C/O–O/Ne white dwarfs. A reliable chemical composition of the core and the chemical transition regions, presented in Fig. 8, is relevant for asteroseimological studies of pulsating white dwarfs. The set of tracks presented here is the first in the literature to cover those core compositions for massive white dwarfs, considering the evolutionary history of the progenitors, and presenting the entire chemical profiles for the sequences.

Our main results are the following:.

(i) From our simulations, we obtained white dwarf sequences characterized with C/O, O/Ne and Ne/O/Mg cores as follows: C/O cores for $M_{\rm WD} \leq 1.088$ $M_\odot$, O/Ne cores for $1.088 < M_{\rm WD} \leq 1.147$ $M_\odot$ and Ne/O/Mg cores for $M_{\rm WD} > 1.147$ $M_\odot$. Note that these values correspond to sequences with initial metallicity $Z = 0.02$. We expect them to vary for different initial metallicities (Doherty et al. 2015) . We compute a sequence with $M_{\rm WD} = 1.13$ $M_\odot$

Downloaded from https://academic.oup.com/mnras/article-abstract/480/2/1547/5065044 by Universidade Federal do Rio Grande do Sul user on 16 January 2019

and $Z = 0.015$ and we find that the chemical structure does not change considerably from the sequence with $Z = 0.02$ and a similar stellar mass in the cooling curve.

(ii) All sequences with $M_{\rm WD} \geq 1.024$ M$_\odot$ experience inward propagating carbon flames with subsequent helium-burning of the outer shells, in the post-AGB stage. The carbon flame for sequences with masses $1.024 \leq M_{\rm WD} \leq 1.147$ M$_\odot$ does not reach the central regions, forming a hybrid C/O–O/Ne white dwarf. For sequences with $M_{\rm WD} > 1.147$ M$_\odot$, the carbon flame reaches the centre of the model producing a Ne/O/Mg core. Our hybrid models present an O/Ne core surrounded by a triple layer of oxygen–carbon–helium, differing from the work of Denissenkov et al. (2013) who reported a C/O core surrounded by an O/Ne zone for hybrid C/O/Ne super-AGB stars.

(iii) Our choice of the Coulomb coupling parameter for crystallization $\Gamma_{\rm full} = 220$, based on the latest asteroseismology results, instead of the MESA default $\Gamma = 175$, can increase the cooling times by ≈0.26 Gyr and decrease the effective temperature at the onset of crystallization by ≈2000 K.

(iv) The amount of hydrogen left at the envelope of a white dwarf has an important affect when determining the stellar mass and the cooling times. Even low quantities of hydrogen, such as those expected for massive white dwarfs, can affect the radii and cooling times. In particular, our H-atmosphere sequences show cooling times ∼0.23–0.66 Gyr larger at $T_{\rm eff} \approx 10\,000$ K, depending on stellar mass, when compared to He-atmosphere sequences with the same mass.

(v) The derived masses for a selection of 252 massive stars from the SDSS DR12 catalogue (Kepler et al. 2016) using our simulations are in good agreement with masses computed using the evolutionary tracks of LPCODE (Althaus et al. 2005a; Romero et al. 2012, 2013), except around masses $M_{\rm WD} = 1.05$–$1.088$ M$_\odot$.

## ACKNOWLEDGEMENTS

We acknowledge the valuable report of the anonymous referee. GRL acknowledges support from CAPES-Brazil. ADR and SOK are grateful for support from CNPq and PRONEX-FAPERGS/CNPq (Brazil). This research has made use of NASA's Astrophysics Data System.

## REFERENCES

Ahn C. P. et al., 2014, ApJS, 211, 17
Alastuey A., Jancovici B., 1978, ApJ, 226, 1034
Althaus L. G., Serenelli A. M., Panei J. A., Córsico A. H., García-Berro E., Scóccola C. G., 2005a, A&A, 435, 631
Althaus L. G., García-Berro E., Isern J., Córsico A. H., 2005b, A&A, 441, 689
Althaus L. G., García-Berro E., Isern J., Córsico A. H., Rohrmann R. D., 2007, A&A, 465, 249
Althaus L. G., Panei J. A., Miller Bertolami M. M., García-Berro E., Córsico A. H., Romero A. D., Kepler S. O., Rohrmann R. D., 2009, ApJ, 704, 1605
Althaus L. G., Córsico A. H., Bischoff-Kim A., Romero A. D., Renedo I., García-Berro E., Miller Bertolami M. M., 2010, ApJ, 717, 897
Althaus L. G., Miller Bertolami M. M., Córsico A. H., 2013, A&A, 557, A19
Bedin L. R., Salaris M., King I. R., Piotto G., Anderson J., Cassisi S., 2010, ApJ, 708, L32
Benvenuto O. G., Althaus L. G., 1999, MNRAS, 303, 30
Bloecker T., 1995, A&A, 297, 727
Brooks J., Bildsten L., Schwab J., Paxton B., 2016, ApJ, 821, 28
Brooks J., Schwab J., Bildsten L., Quataert E., Paxton B., 2017a, ApJ, 834, L9
Brooks J., Schwab J., Bildsten L., Quataert E., Paxton B., 2017b, ApJ, 843, 151
Burgers J. M., 1969, Flow Equations for Composite Gases. Academic Press, New York
Camisassa M. E., Althaus L. G., Córsico A. H., Vinyoles N., Serenelli A. M., Isern J., Miller Bertolami M. M., García-Berro E., 2016, ApJ, 823, 158
Camisassa M. E., Althaus L. G., Rohrmann R. D., García-Berro E., Torres S., Córsico A. H., Wachlin F. C., 2017, ApJ, 839, 11
Campos F. et al., 2016, MNRAS, 456, 3729
Catalán S., Isern J., García-Berro E., Ribas I., 2008, MNRAS, 387, 1693
Chen M. C., Herwig F., Denissenkov P. A., Paxton B., 2014, MNRAS, 440, 1274
Choi J., Dotter A., Conroy C., Cantiello M., Paxton B., Johnson B. D., 2016, ApJ, 823, 102
Cox J. P., Giuli R. T., 1968, Principles of Stellar Structure. Gordon and Breach, New York
Cyburt R. H. et al., 2010, ApJS, 189, 240
Denissenkov P. A., Herwig F., Truran J. W., Paxton B., 2013, ApJ, 772, 37
DeWitt H. E., Graboske H. C., Cooper M. S., 1973, ApJ, 181, 439
Doherty C. L., Gil-Pons P., Siess L., Lattanzio J. C., Lau H. H. B., 2015, MNRAS, 446, 2599
Dotter A., 2016, ApJS, 222, 8
Falcon R. E., Winget D. E., Montgomery M. H., Williams K. A., 2010, ApJ, 712, 585
Farmer R., Fields C. E., Timmes F. X., 2015, ApJ, 807, 184
García-Berro E., Isern J., Hernanz M., 1997a, MNRAS, 289, 973
García-Berro E., Ritossa C., Iben I., Jr. 1997b, ApJ, 485, 765
García-Berro E., Torres S., Althaus L. G., Miller Bertolami M. M., 2014, A&A, 571, A56
Gil-Pons P., Doherty C. L., Lau H., Campbell S. W., Suda T., Guilani S., Gutiérrez J., Lattanzio J. C., 2013, A&A, 557, A106
Graboske H., Dewitt H., Grossman A., Cooper M., 1973, ApJ, 181, 457
Hansen B. M. S. et al., 2007, ApJ, 671, 380
Henize K. G., 1976, ApJS, 30, 491
Herwig F., 2000, A&A, 360, 952
Horowitz C. J., Schneider A. S., Berry D. K., 2010, Phys. Rev. Lett., 104, 231101
Hughto J., Horowitz C. J., Schneider A. S., Medin Z., Cumming A., Berry D. K., 2012, Phys. Rev. E, 86, 066413
Iben I. Jr. Kaler J. B., Truran J. W., Renzini A., 1983, ApJ, 264, 605
Iglesias C. A., Rogers F. J., 1996, ApJ, 464, 943
Isern J., Catalan S., Garcia-Berro E., Salaris M., Torres S., 2010, preprint (arXiv:1010.5351)
Istrate A. G., Tauris T. M., Langer N., Antoniadis J., 2014, A&A, 571, L3
Istrate A. G., Marchant P., Tauris T. M., Langer N., Stancliffe R. J., Grassitelli L., 2016, A&A, 595, A35
Istrate A. G., Fontaine G., Heuser C., 2017, ApJ, 847, 130
Itoh N., Totsuji H., Ichimaru S., Dewitt H., 1979, ApJ, 234, 1079
Itoh N., Hayashi H., Nishikawa A., Kohyama Y., 1996, ApJS, 102, 411
Jones S. et al., 2013, ApJ, 772, 150
Kepler S. O., Romero A. D., 2017, European Physical Journal Web of Conferences, 152, 01011
Kepler S. O., Kleinman S. J., Nitta A., Koester D., Castanheira B. G., Giovannini O., Costa A. F. M., Althaus L., 2007, MNRAS, 375, 1315
Kepler S. O. et al., 2015, MNRAS, 446, 4078
Kepler S. O. et al., 2016, MNRAS, 455, 3413
Kippenhahn R., Ruschenplatt G., Thomas H.-C., 1980, A&A, 91, 175
Kleinman S. J. et al., 2013, ApJS, 204, 5
Langer N., 2012, ARA&A, 50, 107
Langer N., Fricke K. J., Sugimoto D., 1983, A&A, 126, 207
Liebert J., Bergeron P., Holberg J. B., 2005, ApJS, 156, 47
McGraw J. T., Starrfield S. G., Liebert J., Green R., 1979, in van Horn H. M., Weidemann V., Savedoff M. P., eds, Proc. IAU Colloq. Vol. 53, White Dwarfs and Variable Degenerate Stars. Kluwer, Dordrecht, p. 377
Należyty M., Madej J., 2004, A&A, 420, 507



Downloaded from https://academic.oup.com/mnras/article-abstract/480/2/1547/5065044 by Universidade Federal do Rio Grande do Sul user on 16 January 2019

Paxton B., Bildsten L., Dotter A., Herwig F., Lesaffre P., Timmes F., 2011, ApJS, 192, 3
Paxton B. et al., 2013, ApJS, 208, 4
Paxton B. et al., 2015, ApJS, 220, 15
Paxton B. et al., 2018, ApJS, 234, 34
Pignatari M. et al., 2016, ApJS, 225, 24
Poelarends A. J. T., Herwig F., Langer N., Heger A., 2008, ApJ, 675, 614
Potekhin A. Y., Chabrier G., 2010, Contributions to Plasma Physics, 50, 82
Prada Moroni P. G., Straniero O., 2002, ApJ, 581, 585
Rebassa-Mansergas A., Rybicka M., Liu X-W., Han Z., García-Berro E., 2015, MNRAS, 452, 1637
Reimers D., 1975, Mémoires of the Société Royale des Sciences de Liège, 8, 369
Reindl N., Rauch T., Parthasarathy M., Werner K., Kruk J. W., Hamann W.-R., Sander A., Todt H., 2014, A&A, 565, A40
Ritter C., Herwig F., Jones S., Pignatari M., Fryer C., Hirschi R., 2018, MNRAS, preprint (arXiv:1709.08677)
Rogers F. J., Nayfonov A., 2002, ApJ, 576, 1064
Romero A. D., Córsico A. H., Althaus L. G., Kepler S. O., Castanheira B. G., Miller Bertolami M. M., 2012, MNRAS, 420, 1462
Romero A. D., Kepler S. O., Córsico A. H., Althaus L. G., Fraga L., 2013, ApJ, 779, 58
Salaris M., García-Berro E., Hernanz M., Isern J., Saumon D., 2000, ApJ, 544, 1036
Salaris M., Althaus L. G., García-Berro E., 2013, A&A, 555, A96
Saumon D., Chabrier G., van Horn H. M., 1995, ApJS, 99, 713
Schaefer B. E., Edwards Z. I., 2015, ApJ, 812, 133
Schneider A. S., Hughto J., Horowitz C. J., Berry D. K., 2012, Phys. Rev. E, 85, 066405
Schoenberner D., 1979, A&A, 79, 108
Schwab J., Bildsten L., Quataert E., 2017, MNRAS, 472, 3390
Segretain L., Chabrier G., Hernanz M., Garcia-Berro E., Isern J., Mochkovitch R., 1994, ApJ, 434, 641
Siess L., 2006, A&A, 448, 717
Siess L., 2007, A&A, 476, 893
Siess L., 2010, A&A, 512, A10
Sun M., Arras P., 2018, ApJ, 858, 14
Thoul A. A., Bahcall J. N., Loeb A., 1994, ApJ, 421, 828
Timmes F. X., Swesty F. D., 2000, ApJS, 126, 501
Tremblay P.-E., Ludwig H.-G., Steffen M., Freytag B., 2013, A&A, 559, A104
Ulrich R. K., 1972, ApJ, 172, 165
van Horn H. M., 1968, ApJ, 151, 227
Van Horn H. M., 1969, Phys. Lett. A, 28, 706
Vassiliadis E., Wood P. R., 1993, ApJ, 413, 641
Wang B., Podsiadlowski P., Han Z., 2017, MNRAS, 472, 1593
Winget D. E., Hansen C. J., Liebert J., van Horn H. M., Fontaine G., Nather R. E., Kepler S. O., Lamb D. Q., 1987, ApJ, 315, L77
Winget D. E., Kepler S. O., Kanaan A., Montgomery M. H., Giovannini O., 1997, ApJ, 487, L191
Woosley S. E., Heger A., 2015, ApJ, 810, 34

## APPENDIX: CHEMICAL PROFILES AT THE END OF THE COOLING SEQUENCE

Here, we present the chemical profiles of all our models for H- and He-atmosphere white dwarfs. Fig. A1 shows the chemical profiles for H and He atmospheres (left and right columns, respectively) . Each row presents H- and He-atmosphere models for the same mass. All chemical profiles presented in this section are for $T_{\rm eff} \approx 10\,000$ K.

Downloaded from https://academic.oup.com/mnras/article-abstract/480/2/1547/5065044 by Universidade Federal do Rio Grande do Sul user on 16 January 2019

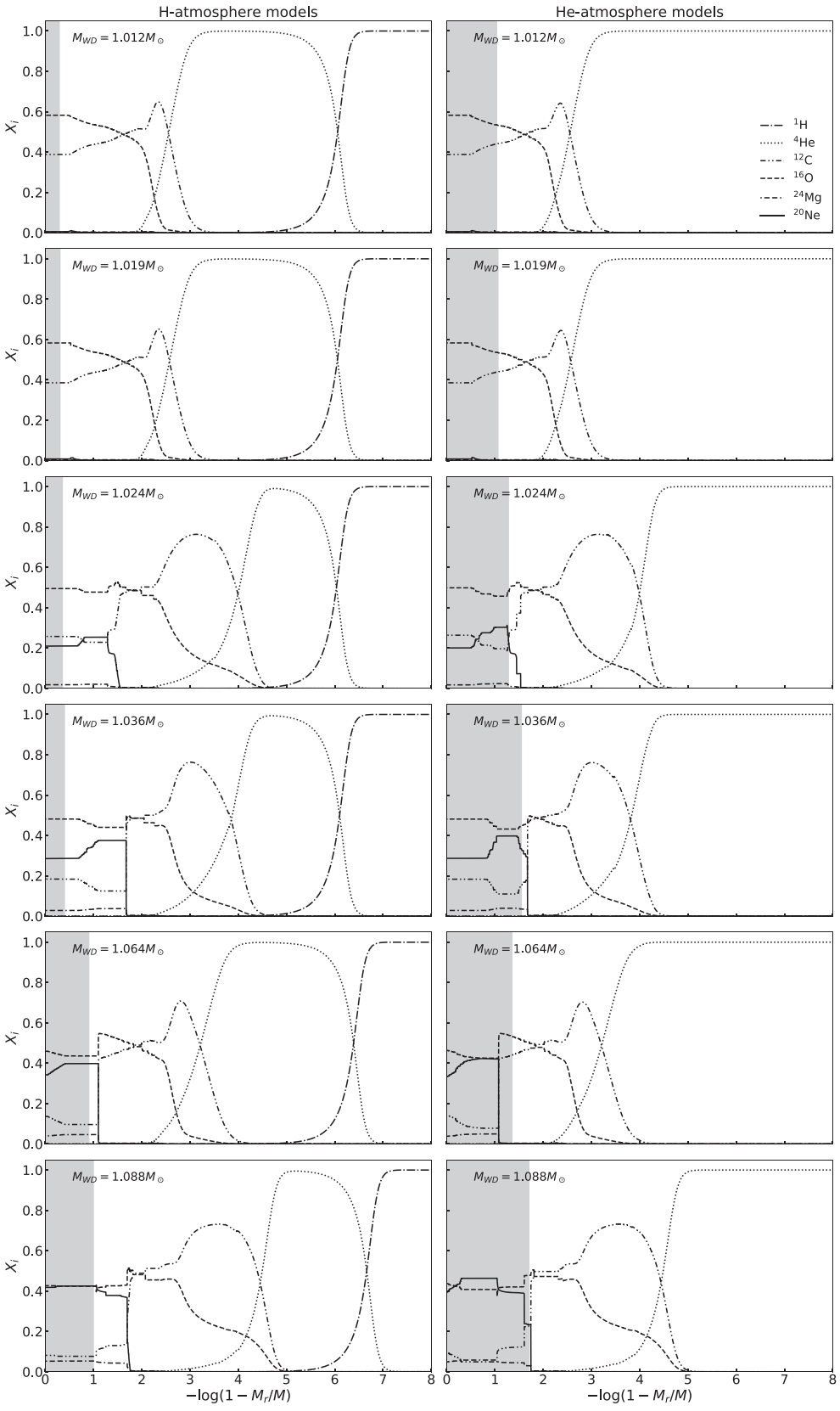


**Figure A1.** Chemical profiles in terms of outer mass fractions for H-atmosphere (left) and He-atmosphere (right) models at $T_{\rm eff} \approx 10\,000$ K in the cooling sequence. The shaded regions denote the crystallized portion of the core. Each row presents H (left) and He (right) atmospheres for the same mass.

Downloaded from https://academic.oup.com/mnras/article-abstract/480/2/1547/5065044 by Universidade Federal do Rio Grande do Sul user on 16 January 2019

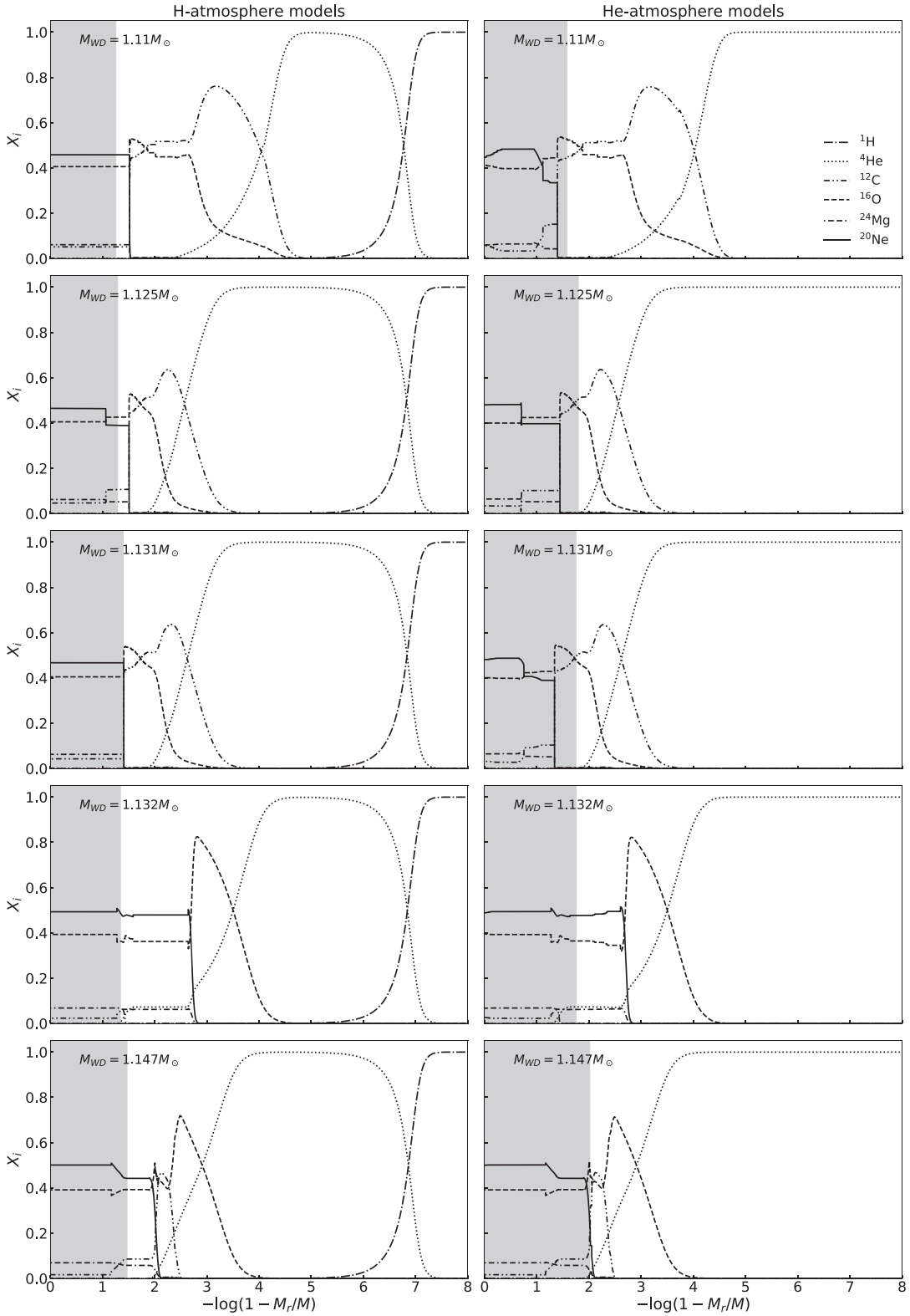


**Figure A1** *– continued*

Downloaded from https://academic.oup.com/mnras/article-abstract/480/2/1547/5065044 by Universidade Federal do Rio Grande do Sul user on 16 January 2019

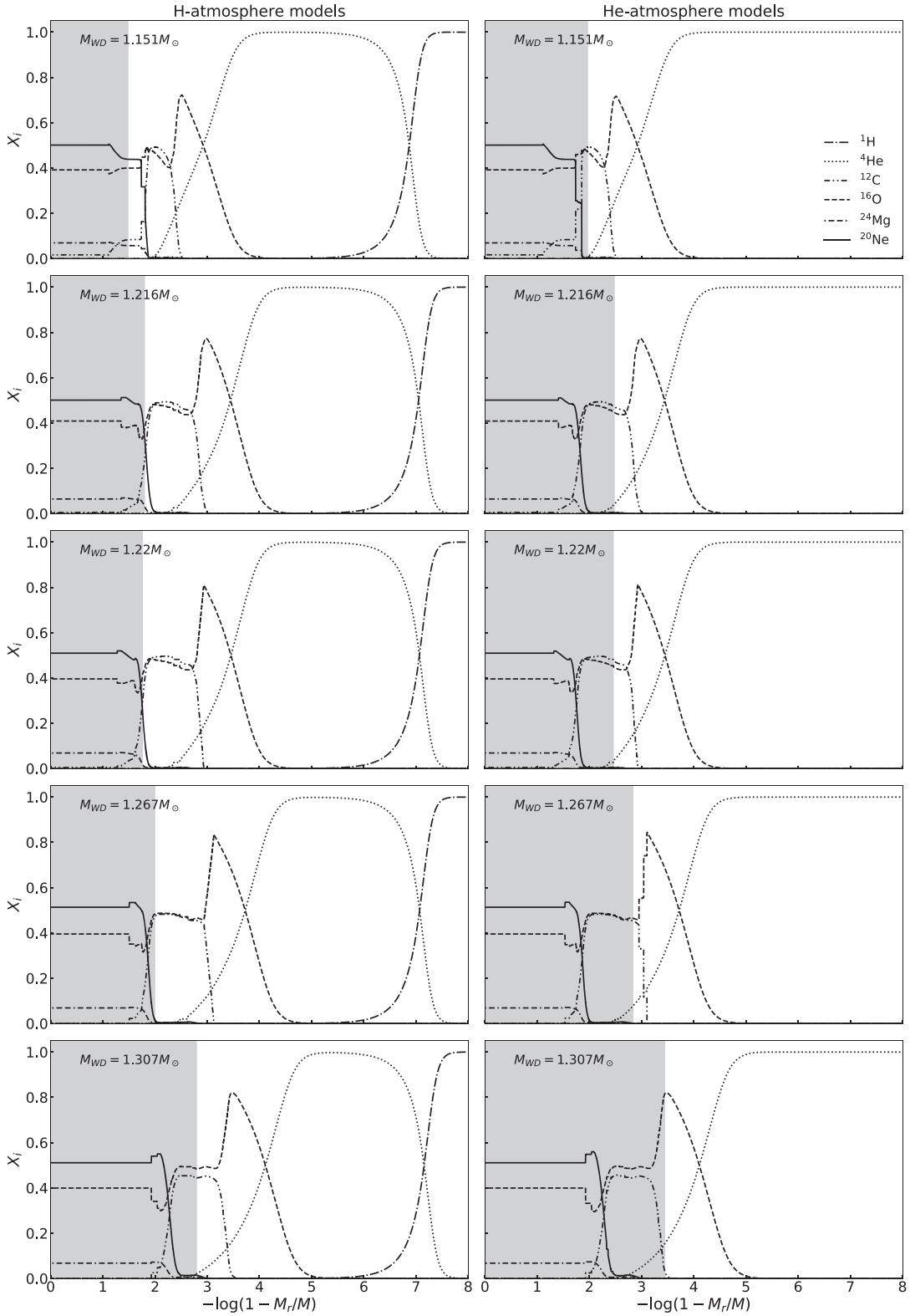


**Figure A1** – *continued*

This paper has been typeset from a TEX/LATEX file prepared by the author.

Downloaded from https://academic.oup.com/mnras/article-abstract/480/2/1547/5065044 by Universidade Federal do Rio Grande do Sul user on 16 January 2019